jove

Probing Surface Electrochemical Activity of Nanomaterials using a Hybrid Atomic Force Microscope-Scanning Electrochemical Microscope (AFM-SECM)

Xiaonan Shi[1], **Qingquan Ma**[1], **Taha Marhaba**[1], **Wen Zhang**[1]

[1] Department of Civil and Environmental Engineering, New Jersey Institute of Technology

Corresponding Author

Wen Zhang
wzhang81@njit.edu

Citation

Shi, X., Ma, Q., Marhaba, T., Zhang, W. Probing Surface Electrochemical Activity of Nanomaterials using a Hybrid Atomic Force Microscope-Scanning Electrochemical Microscope (AFM-SECM). *J. Vis. Exp.* (), e61111, doi:10.3791/61111 (2020).

Date Published

June 11, 2020

DOI

10.3791/61111

URL

jove.com/video/61111

Abstract

Scanning electrochemical microscopy (SECM) is used to measure the local electrochemical behavior of liquid/solid, liquid/gas and liquid/liquid interfaces. Atomic force microscopy (AFM) is a versatile tool to characterize micro- and nanostructure in terms of topography and mechanical properties. However, conventional SECM or AFM provides limited laterally resolved information on electrical or electrochemical properties at nanoscale. For instance, the activity of a nanomaterial surface at crystal facet levels is difficult to resolve by conventional electrochemistry methods. This paper reports the application of a combination of AFM and SECM, namely, AFM-SECM, to probe nanoscale surface electrochemical activity while acquiring high-resolution topographical data. Such measurements are critical to understanding the relationship between nanostructure and reaction activity, which is relevant to a wide range of applications in material science, life science and chemical processes. The versatility of the combined AFM-SECM is demonstrated by mapping topographical and electrochemical properties of faceted nanoparticles (NPs) and nanobubbles (NBs), respectively. Compared to previously reported SECM imaging of nanostructures, this AFM-SECM enables quantitative assessment of local surface activity or reactivity with higher resolution of surface mapping.

Introduction

Characterization of electrochemical (EC) behavior can provide critical insights into the kinetics and mechanisms of interfacial reactions in diverse fields, such as biology[1,2], energy[3,4], material synthesis[5,6,7], and chemical process[8,9]. Traditional EC measurements including electrochemical impedance spectroscopy[10], electrochemical noise methods[11], galvanostatic intermittent titration[12], and cyclic voltammetry[13] are usually performed at macroscopic scale and provide a surface-average response. Thus, it is difficult to extract information on how electrochemical-activity is distributed across a surface, but local scale surface properties in nanoscale are especially

important where nanomaterials are widely used. Therefore, new techniques capable of simultaneously capturing both nanoscale multidimensional information and electrochemistry are highly desirable.

Scanning electrochemical microscopy (SECM) is a widely used technique for measuring the localized electrochemical activity of materials at micro- and nanoscales[14]. Typically, SECM uses an ultra-microelectrode as a probe for detecting electroactive chemical species as it scans a sample surface to spatially resolve local electrochemical properties[15]. The measured current at the probe is produced by reduction (or oxidation) of the mediator species, and this current is an indicator of the electrochemical reactivity at the surface of the sample. SECM has evolved significantly after its first inception in 1989[16,17] but it is still challenged by two main limitations. Since EC signals are typically sensitive to tip-substrate interaction characteristics, one limitation of SECM is that keeping the probe at a constant height prevents a direct correlation of electrochemical activity with the surface landscape, due to the convolution of topography with the collected EC information[18]. Second, it is difficult for a commercial SECM system to obtain sub-micrometer (μm) image resolution as the spatial resolution is partially determined by the probe dimensions, which is on the micrometer scale[19]. Therefore, nanoelectrodes, the electrodes with a diameter in the nanometer range, are increasingly used in SECM to achieve a resolution below the sub-micrometer scale[20,21,22,23].

To provide a constant tip-substrate distance control and obtain a higher spatial electrochemical resolution, several hybrid techniques of SECM have been used, such as ion conductance positioning[24], shear force positioning[25], alternating current SECM[26], and atomic force microscopy (AFM) positioning. Among these instrumentations, SECM integrating AFM positioning (AFM-SECM) has become a highly promising approach. As AFM can provide fixed tip-substrate distances, the integrated AFM-SECM technique enables simultaneous acquisition of nanoscale surface structural and electrochemical information through mapping or sample sweeping with the sharp AFM tips. Since the first successful operation of AFM-SECM by MacPherson and Unwin in 1996[27], significant improvements have been achieved on probe design and fabrication, as well as its applications in various research fields such as electrochemistry in chemical and biological processes. For example, AFM-SECM has been implemented for imaging composite material surfaces, such as noble metal nanoparticles[28], functionalized or dimensionally stable electrodes[29,30], and electronic devices[31]. AFM-SECM can map the electrochemically active sites from the tip current image.

Simultaneous topographical and electrochemical measurements could also be achieved by other techniques such as conductive AFM[32,33,34,35], electrochemical AFM (EC-AFM)[36,37,38,39], scanning ion conductance microscopy-scanning electrochemical microscopy (SICM-SECM)[24,40], and scanning electrochemical cell microscopy (SECCM)[41,42] The comparison between these techniques has been discussed in a review paper[1]. The aim of the present work was to employ SECM-AFM to demonstrate the electrochemical mapping and measurement on faceted crystalline cuprous oxide nanomaterials and nanobubbles in water. Faceted nanomaterials are widely synthesized for metal oxide catalysts in clean energy applications because the facets with distinctive crystallographic features have distinctive surface atomic structures and further dominate their catalytic properties. Moreover, we also measured

and compared the electrochemical behavior at the liquid/gas interfaces for surface nanobubbles (NBs) on gold substrates. NBs are bubbles with a diameter of <1 μm (also known as ultrafine bubbles)[43], and they elicit many intriguing properties[44,45], including long residence times in the solutions[46,47] and higher efficiency of gas mass transfer[46,48]. Furthermore, the collapse of NBs creates shock waves and the formation of hydroxyl radicals (•OH)[49,50,51,52]. We measured the electrochemical reactivity of oxygen NBs in the solution to better understand the fundamental chemical properties of NBs.

Protocol

1. Sample preparation

1. **Preparation of faceted Cu_2O nanoparticles and deposition on silicon substrate**
    1. Dissolve 0.175 g of $CuCl_2 \cdot 2H_2O$ (99.9%) into 100 mL of deionized (DI) water to generate an aqueous solution of 10 mM $CuCl_2$.
    2. Add 10.0 mL of 2.0 M NaOH and 10 mL of 0.6 M ascorbic acid dropwise into the $CuCl_2$ solution.
    3. Heat the solution in a 250 mL round-bottom flask under constant stirring in a 55 °C water bath for 3 h.
    4. Collect the resulting precipitate by centrifugation (5,000 x *g* for 15 min), followed by washing with DI water 3 times and ethanol twice to remove the residual inorganic ions and polymers.
    5. Dry precipitate in vacuum at 60 °C for 5 h[53].
    6. Use the prepared silicon wafer as the substrate to deposit Cu_2O nanoparticles as illustrated in **Figure 1A** using epoxy to ensure the testing.

        Caution: The silicon wafer (Ø3" Silicon wafer, Type P/<111>) was cut into a single piece of 38 mm x 38 mm, followed by washing using ethanol, methanol and DI water to remove organic and inorganic contaminants.
    7. Directly deposit 10 μL of epoxy on the cleaned silicon wafer using a pipette tip and tile with a clean glass slide. After about 5 min, drop 10 μL of the nanoparticles/water suspension (10 mg L^{-1}) on different epoxy-coated silicon wafer substrates, separately. The four different red spots shown in **Figure 1B** indicate the potential position of the deposited nanoparticles.
    8. Vacuum dry the substrate at 40 °C for 6 h.
    9. Place the sample substrate into the EC sample cell (**Figure 4**) to be filled with 1.8 mL of a 0.1 M KCl containing 10 mM $Ru(NH_3)_6Cl_3$ (98%).
2. **Preparation of NBs**
    1. Generate oxygen nanobubbles by direct injection of compressed oxygen (purity 99.999%) through a tubular ceramic membrane (100 nm pore size, WFA0.1) into DI water.

        NOTE: The gas was injected continuously under a pressure of 414 kPa and a flow of 0.45 $L \cdot m^{-1}$ until reaching stable bubble size distribution as reported elsewhere[54].
    2. Add 1.8 mL of the water suspension of NBs on a gold substrate in the EC sample cell and stabilize for 10 min.

        NOTE: Fresh 40 mm x 40 mm gold plates (Au on Si) were used as the substrate to immobilize NBs.
    3. Decant 0.9 mL of NB suspension and replace with 0.9 mL of a 10 mM $Ru(NH_3)_6Cl_3$ solution in 0.1 M KCl.

2. Setup of AFM-SECM

NOTE: AFM was used in the presented AFM-SECM measurements. To perform the EC analyses, the AFM was equipped with a bipotentiostat and SECM accessories. As shown in **Figure S1**, the bipotentiostat was connected to the AFM controller and both the potentiostat and AFM were connected to the same computer. The accessories include an SECM chuck, an SECM probe holder with protective boot, and a strain-release module with a resistance selector (10 MΩ resistance was used) to limit the maximum current flow[55] . As shown in **Figure 2**, the AFM-SECM probes have a tip radius of 25 nm and a tip height of 215 nm. The sample acted as a working electrode, which shares the same pseudo-reference using the Ag wire electrode (25 mm diameter) and the counter electrode of a Pt wire (25 mm in diameter). The probe and the sample could be biased at different potentials (vs the Ag wire pseudo-reference electrode) to enable different redox reactions. In the presented work, the tip reduces the $[Ru(NH_3)_6]^{3+}$ to $[Ru(NH_3)_6]^{2+}$ at -400 mV versus an Ag wire pseudo-reference electrode.

1. Replace the existing sample chuck with SECM chuck and screw the chuck in place using two M3 x 6 mm socket head cap screws and a 2.5 mm hex wrench (**Figure 3A**).
2. Connect the temperature control cable to the SECM chuck, and connect the low-noise SECM cables to the spring connector block (color to color) and switch block (**Figure 3B**).
   NOTE: The switch needs to be kept on the right side during SECM testing.
3. Install the strain-release module onto the AFM scanner and also connect it to the working electrode connector on the spring connector block with extension cable (**Figure 3C**).
4. Assemble the EC sample cell.
   1. Put the insert onto the top ring (**Figure 4A**).
   2. Assemble two O-rings onto the bottom groove and top groove of the insert, respectively (**Figure 4B** and **Figure 4C**).
   3. Put a glass cover onto the top ring top and then tighten by four screws lightly and diagonally (**Figure 4D**).
   4. Use a hard sharp wire with a 24 mm diameter (**Figure 4E**) to poke two holes in the O-ring through two channels of plastic part on top ring (**Figure 4F**).
   5. Insert Ag wire and Pt wire through the hole on the O-ring, and curve the Pt wire to a circle in EC sample cell as shown in **Figure 4G**.
   6. To seal the EC sample cell top part, press the assembled EC sample cell down on the EC sample cell bottom to make the O-ring fully contact the glass cover (**Figure 4H**).
   7. Place the top part of the EC sample cell upside-down and face the test sample (or substrate) downward so that the spring-loaded pins (pogo pins) touch the sample surface as shown in **Figure 4I** and **Figure 4J**. The test sample should be covering the O-ring to make EC sample cell bottom part seal.
   8. Put the EC sample cell bottom on and tighten diagonally with right length screw (**Figure 4K**).

3. Operation of AFM-SECM

1. **Initialization of the AFM and bipotentiostat instruments**

1. Double click the two software icons to initialize the AFM system and the bipotentiostat control interface.

2. **Loading SECM Probe**

    1. Prepare the ESD field service package including antistatic pad, electrostatic discharge (ESD) protective probe stand, wearable anti-static gloves and wrist strap (**Figure 5A**). **Figure 5B** shows the connection of the ESD monitor with wrist strap.
    NOTE: The ESD monitor beeps when the red pad is connected with ground. The beep will stop when user wears the wrist strap.

    2. To prevent AFM scanner from exposure to liquid, use a protective boot (**Figure 6A**) during AFM-SECM testing. Put the probe holder onto the ESD protective probe stand (**Figure 6B**). Use a pair of plastic tweezers to attach the protective boot to the tip holder (**Figure 6C**). Then, align the small cut in the protective boot to the notch in the probe holder as illustrated in **Figure 6D**.

    3. Open the box of AFM-SECM probes (**Figure 7A**) using a tip tweezer (green color) to grab the probe from both sides of the grooves (**Figure 7B**). While using the disk gripper (silver color) to hold the probe holder on the stand, put the probe wire into the hole of the stand, and then slide the probe into the slot of the probe holder (**Figure 7C**). After the probe is inside the slot, use the flat end of the tweezer to push it in. Make sure the probe is completely in the tip holder (**Figure 7D**).

    4. As shown in **Figure 8A**, attach the whole probe holder (including the holder-boot) to the scanner.

    5. Use the Teflon tip tweezer to grab the wire right below the copper ring and connect it to the module (**Figure 8B**).

    6. Put the scanner back to the dovetail.

3. **Loading the sample cell**

    1. After assembling the test sample (or substrate) in the EC sample cell, which was mentioned in Section 2.4, put the EC sample cell on the central point of the SECM chuck and the pseudo-reference electrode (Ag wire) and connect the counterelectrode (Pt wire) to the spring connector block (**Figure 3**). The EC sample cell is magnetically attached to the chuck.

4. **SECM software preparation before imaging**

    1. In the AFM-SECM software, select SECM-PeakForce QNM to load the workspace (**Figure S2**).

    2. In **Setup**, load the SECM probe, and then align a laser on the tip using an alignment station.

    3. Go to **Navigation** (**Figure S3**). Move the scanner downwards slowly to focus on the sample surface. Adjust the position of EC sample cell slightly to make sure the scanner would not touch the glass cover of EC sample cell while moving. After focusing on the sample, click **Update Blind Engage Position**.
    Caution: Different samples have different heights, so it is necessary to update the blind engage position after changing a sample.

    4. Click **Move to Add Fluid Position**.

    5. Add ~1.8 mL of the buffer solution into the EC sample cell, to make sure the level of the solution is lower than the glass cover. If the water level is over the glass cover, water can creep to the scanner and cause an electric short and break the scanner. Wait for another

5 minutes and use a pipette to agitate the solution to remove bubbles.

NOTE: The buffer solution (10 mM $[Ru(NH_3)_6]^{3+}$ with supporting electrolyte of 0.1 M KCl) should be constantly stored in a refrigerator after preparation. Use a syringe with filter (no larger than 1 µm pore size) to filter the solution before using it.

6. Click **Move to Blind Engage Position**. The tip will move back into the buffer solution. Adjust the laser slightly to make sure the laser is aligned on the tip.

7. Open CHI software. As shown in **Figure S4**, click on the **Technique** command on the toolbar to open up the tech selector and select **Open Circuit Potential – Time**. Use the default setting (Run time as 400 s) for OCP measurement and run the OCP measurement.

   NOTE: The potential showed in OCP test should be near zero stably.

8. Click the **Technique** command again and run **Cyclic Voltammetry (CV)**, as shown in **Figure S5 and Figure S6**.

   NOTE: Set up the parameters as below. Set “sweep segments” to a larger number if needed. The “init E/Final E” should be as the same as the potential value from OCP measurement and “High E” and “Low E” could be +0.3 V or −0.3 V of “ init E/Final E”, respectively. Here we use 0 V as initial and high E and -0.4 V as Low and Final E. The scan rate was 0.05 V/s and the sensitivity was 1 e-009. Run the CV test, the highest current (i) measured here should be 0.3-1.2 nA for 10 mM $[Ru(NH_3)_6]^{3+}$.

5. **SECM Imaging**

1. Go back to the AFM-SECM software. Since the tip is already in the liquid, click **Engage**.

2. After scanning, turn on lift mode (Lift by Sensor) with a lift height of 100 nm and adjust the lift height based on the sample roughness.

3. In CHI software, run a chronoamperometry with parameters shown in **Figure S7**. Set the initial E as -0.4 V, the pulse width as 1000 seconds (which is the maximum number accepted by the system), and the sensitivity the same with CV scan.

   NOTE: The chronoamperometry technique was chosen because of the absence of amperometric i-t technique in the presented bi-potentiostat.

4. With the CHI program running, go back to AFM-SECM software, check the real-time reading on the strip chart and click on **Start** (**Figure S8**). The reading will be updated in real-time. Then both topography imaging and current imaging process will begin. Save images in the AFM-SECM software.

6. **Check approach curve**

1. Engage the tip on sample or substrate region with a scan size of 1 µm.

2. Run the **Chronoamperometry** as mentioned in 3.5.3.

3. Go back to AFM-SECM Software and select the command **Go To Ramp**.

4. Click **Ramp**. An approach curve would be recorded in the AFM-SECM software.

7. **Tip cleaning**

1. Using the EC sample cell as a clean water container. Move the tip in and out of the liquid using blind engage functions in the navigation panel. Change the clean water three times. After this three-time cleaning, using clean wipes to carefully remove residual water from

the probe holder and put the probe back in the probe box.

Caution: After imaging, the AFM-SECM probe needs to be carefully cleaned. Never use water coming out from the wash bottle to clean the probe as the electrostatic charge might damage the probe.

Representative Results

Topography and current imaging of ONBs by AFM-SECM

Previous studies that characterized NBs with AFM only reported topography images to reveal the size and distribution of NBs immobilized on a solid substrate[56,57]. The experiments here revealed both morphological and electrochemical information. Individual oxygen nanobubbles (ONBs) can be clearly identified in **Figure 9**, which provides the topography as well as the tip current mapping or information. The tip current was generated by the redox reaction of $[Ru(NH_3)_6]^{3+}$ that is reduced to $[Ru(NH_3)_6]^{2+}$ at the tip under a bias potential at -0.4 V, as depicted in **Figure 9C**. A comparison of the topography and current image shows the good correlation between the locations of the NBs and the current spots. This result confirms that ONBs could facilitate the diffusion and mass transfer of $[Ru(NH_3)_6]^{3+}$ from the bulk solution to the tip area[58] and result in a higher current (relative to the substrate background current of 6 pA) when the AFM-SECM tip scanned over NBs[59].

Topography and current imaging of Cu_2O NPs by AFM-SECM

The topography and current images of Cu_2O nanoparticles are presented in **Figure 10**. The tip current was generated due to the redox reaction of $[Ru(NH_3)_6]^{3+}$, which are also reduced at the tip with a potential at -0.4 V, as depicted in **Figure 10C**. The nanoparticle is about 500-1000 nm in size. The presented topography image was processed with a 1st order flattening treatment. The particle size determined by AFM is comparable to that obtained from the SEM image. The length or width is slightly larger than the height of the nanoparticles (around 500 nm) due to the tip convolution effect, a well-known artifact in the AFM imaging process that causes the overestimation of the object dimension by a finite-sized AFM tip[60]. In this study, as the Cu_2O nanoparticle has a sharp octahedron shape, the AFM tip may fail to touch the steep sidewall and bottom, and this convolution effect can account for many lateral broadening of the surface[61]. **Figure 10B** indicates that the nanoparticle visible in the topography image is associated with evident electric current "spot" in current image, whereas the background current (~10 pA) corresponds to the flat silicon substrate.

CV and Approach curves of Cu_2O NPs

Figure 11A shows five representative CV curves of the AFM-SECM tip with the tip at around 1 mm away from the substrate in 10 mM $[Ru(NH_3)_6]^{3+}$ and 0.1 M KCl. The diffusion-limited tip current (~1.2 nA) did not decrease with time. **Figure 11A** shows the CV curve at a scan rate as 50 mV s^{-1}, which confirms the bias potential of -0.4 V vs Ag/AgCl led to the maximum plateau tip current due to the reduction reaction of $[Ru(NH_3)_6]^{3+}$.

Figure 11B shows the changes of the tip current as the tip move towards the sample surface. The AFM-SECM tip approached the substrate surface in the Z direction until it reached a setpoint (5 nN in this work) that indicates the physical tip-substrate contact or bending as a result of the contact[62,63]. The current on the plots were normalized to i_0 (i_0 =3.385 nA), which is defined as the tip current measured when the tip is 1 μm above the sample surface. The tip was biased at −0.4 V vs Ag/AgCl in electrolyte containing 10

mM $[Ru(NH_3)_6]^{3+}$ and 0.1 M KCl. The normalized tip current increased with the decreasing tip-sample distance. At <8 nm, the tip was in contact with the nanoparticle surface and the normalized tip current increased sharply, probably because the negatively charged Si surface would result in an increased local concentration of $[Ru(NH_3)_6]^{3+}$ near the surface.

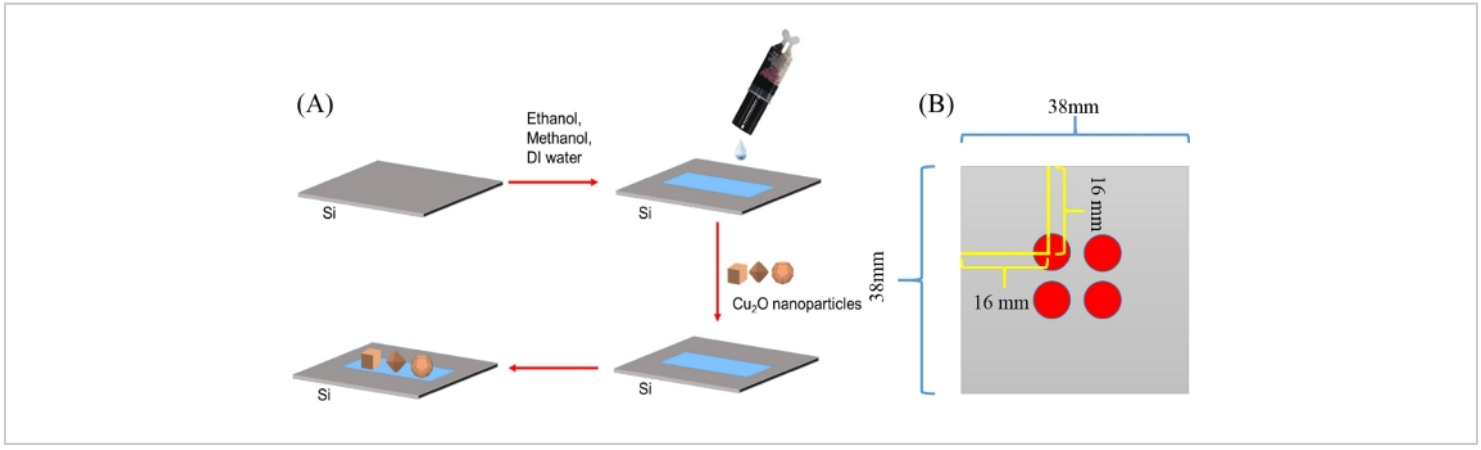

Figure 1: Deposition of Cu_2O nanoparticles on a silicon wafer. Please click here to view a larger version of this figure.

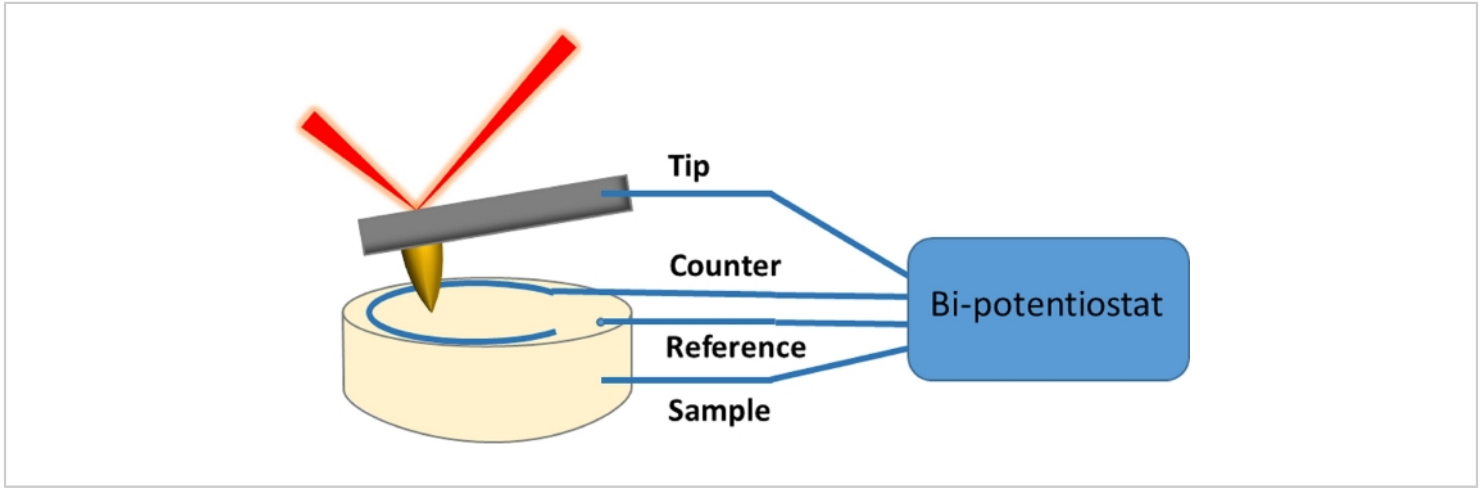

Figure 2: Schematic of AFM-SECM system Please click here to view a larger version of this figure.

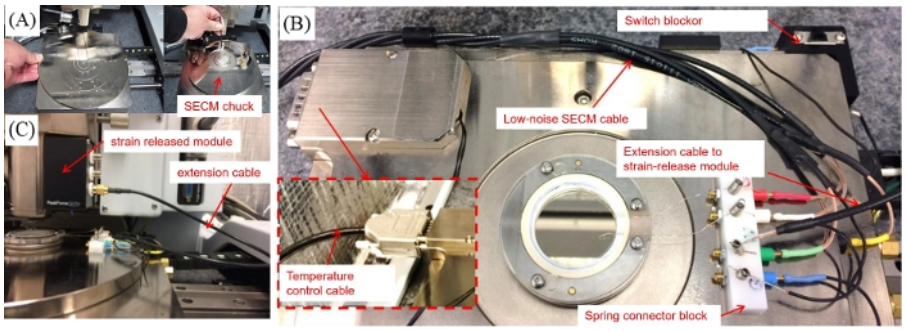

Figure 3: Installation procedure for SECM chuck and other accessories. Please click here to view a larger version of this figure.

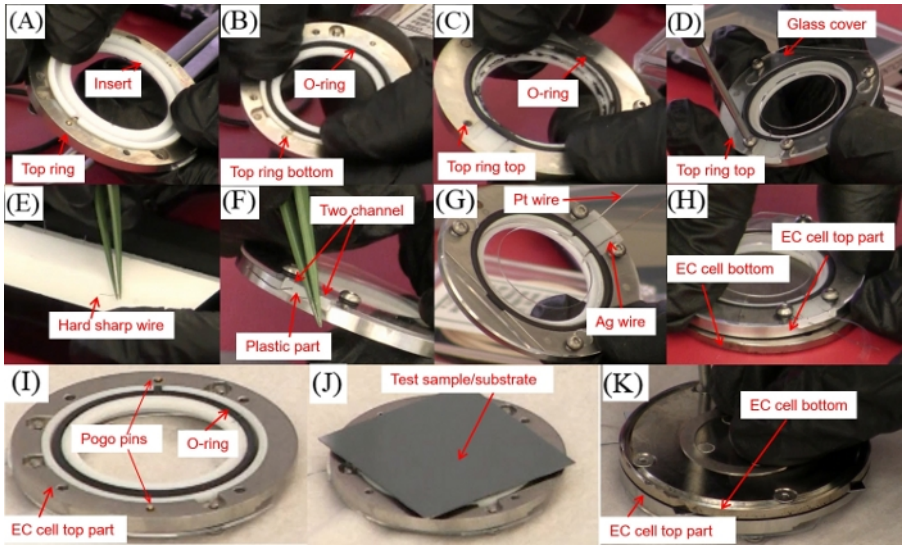

Figure 4: Assemblage procedure of the EC sample cell. Please click here to view a larger version of this figure.

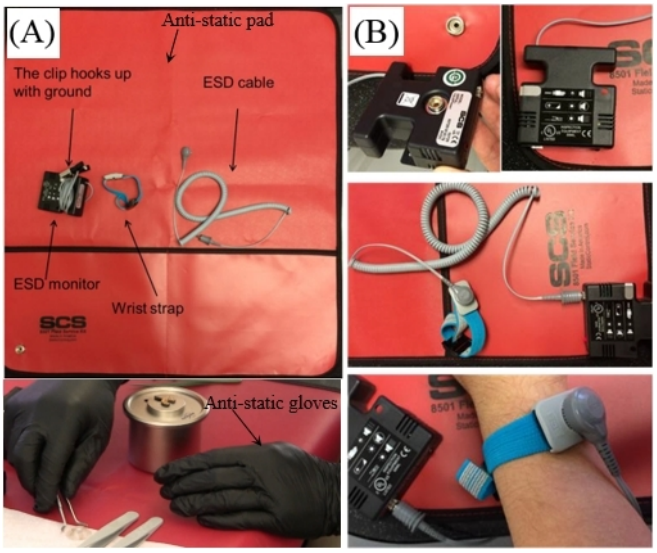

Figure 5: The ESD field service package.

(**A**) Parts of ESD protective parts; (**B**) Connections of ESD monitor, wrist strap and ground wire. Please click here to view a larger version of this figure.

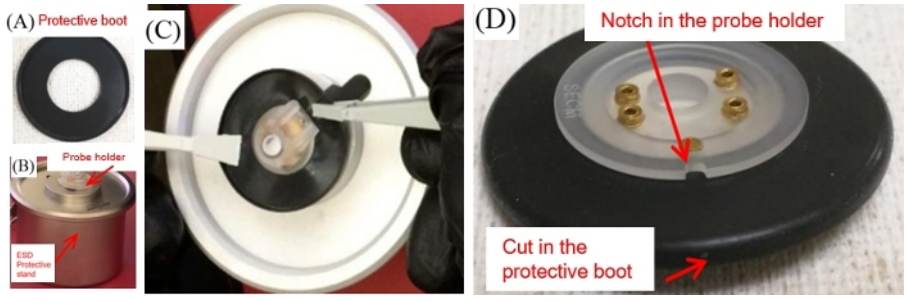

Figure 6: Attachment procedure for the protective boot onto the probe holder Please click here to view a larger version of this figure.

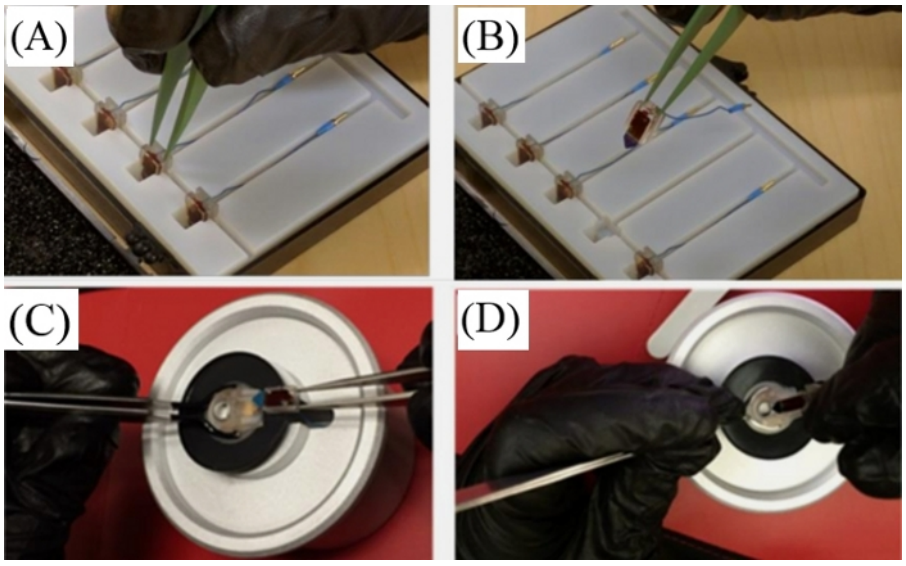

Figure 7: Loading the SECM probe to the probe holder Please click here to view a larger version of this figure.

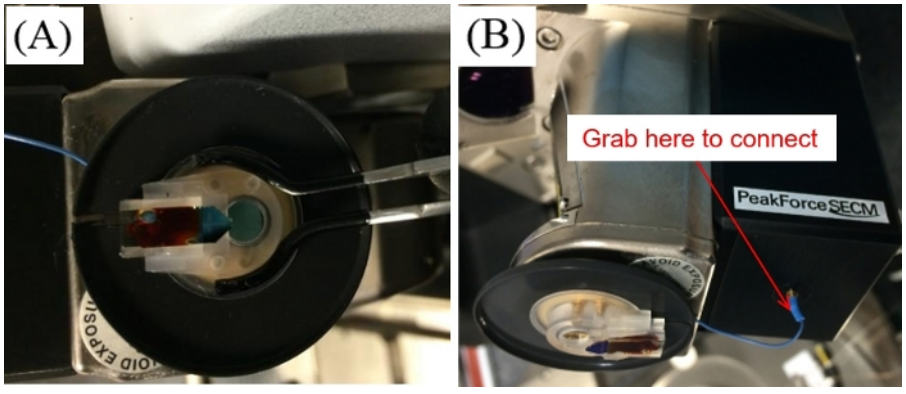

Figure 8: The SECM Probe.

(**A**) Attach the probe-holder-boot assembly to the scanner; (**B**) Connection of probe to the strain released module. Please click here to view a larger version of this figure.

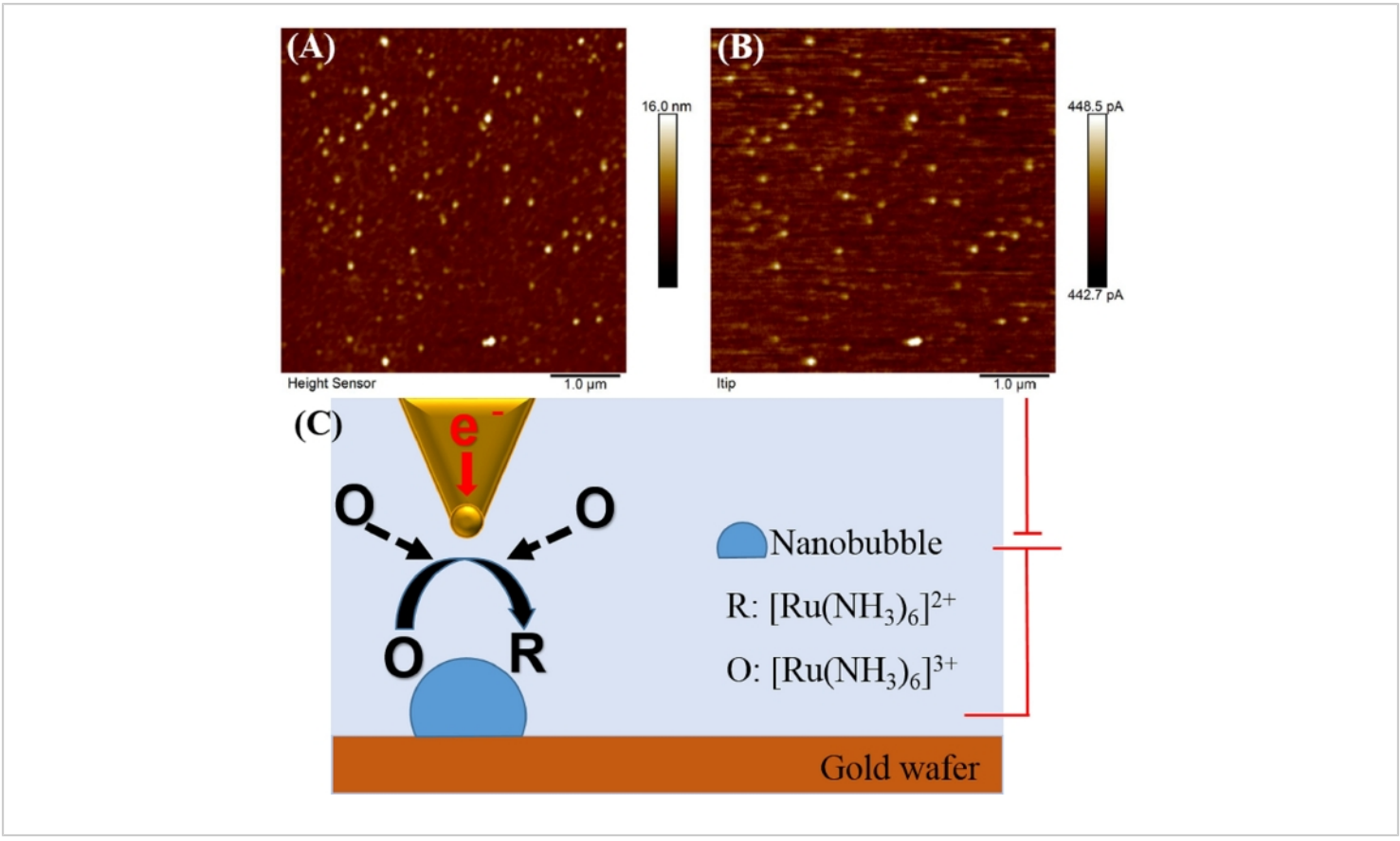

Figure 9: Simultaneously acquired topography (A) and tip current (B) images of oxygen NBs in electrolyte containing 10 mM $[Ru(NH_3)_6]^{3+}$ and 0.1 M KCl.

The tip (end tip radius is 25nm) was biased at -0.4V. (C) Schematic illustration of AFM-SECM measurement of NBs Please click here to view a larger version of this figure.

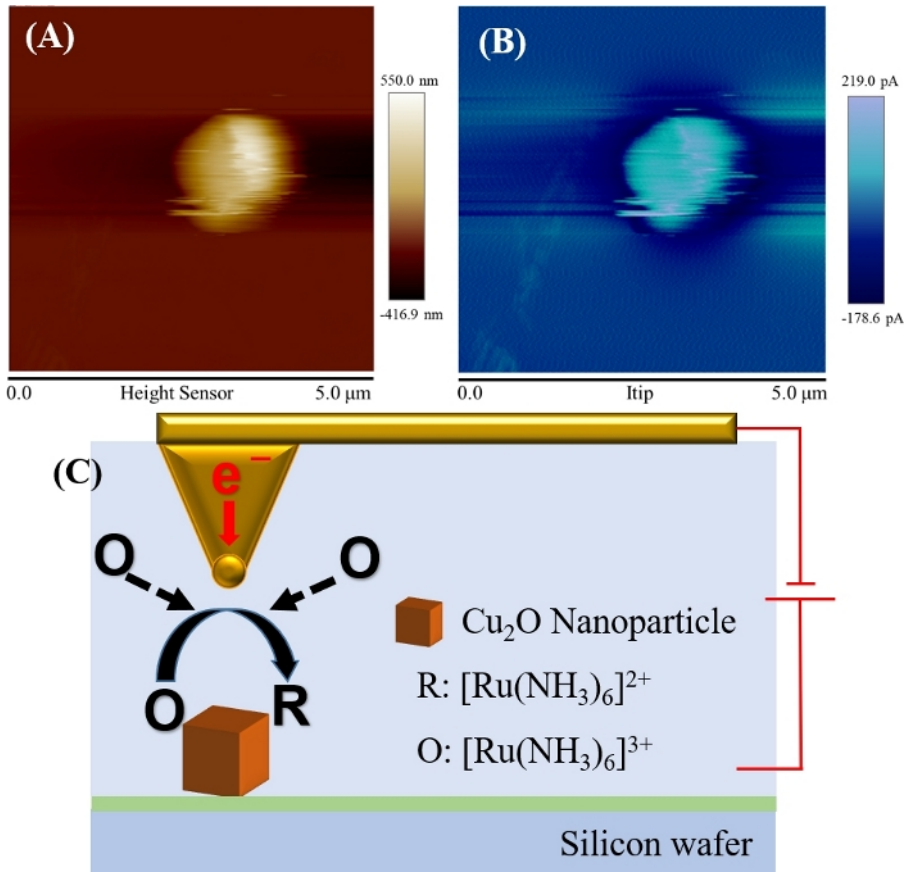

Figure 10: Simultaneously acquired topography (A) and tip current (B) images of Cu_2O nanoparticles in electrolyte containing 10 mM $[Ru(NH_3)_6]^{3+}$ and 0.1 M KCl.

The tip (end tip radius is 25nm) was biased at -0.4V (C) Schematic illustration of AFM-SECM measurement of NPs. Please click here to view a larger version of this figure.

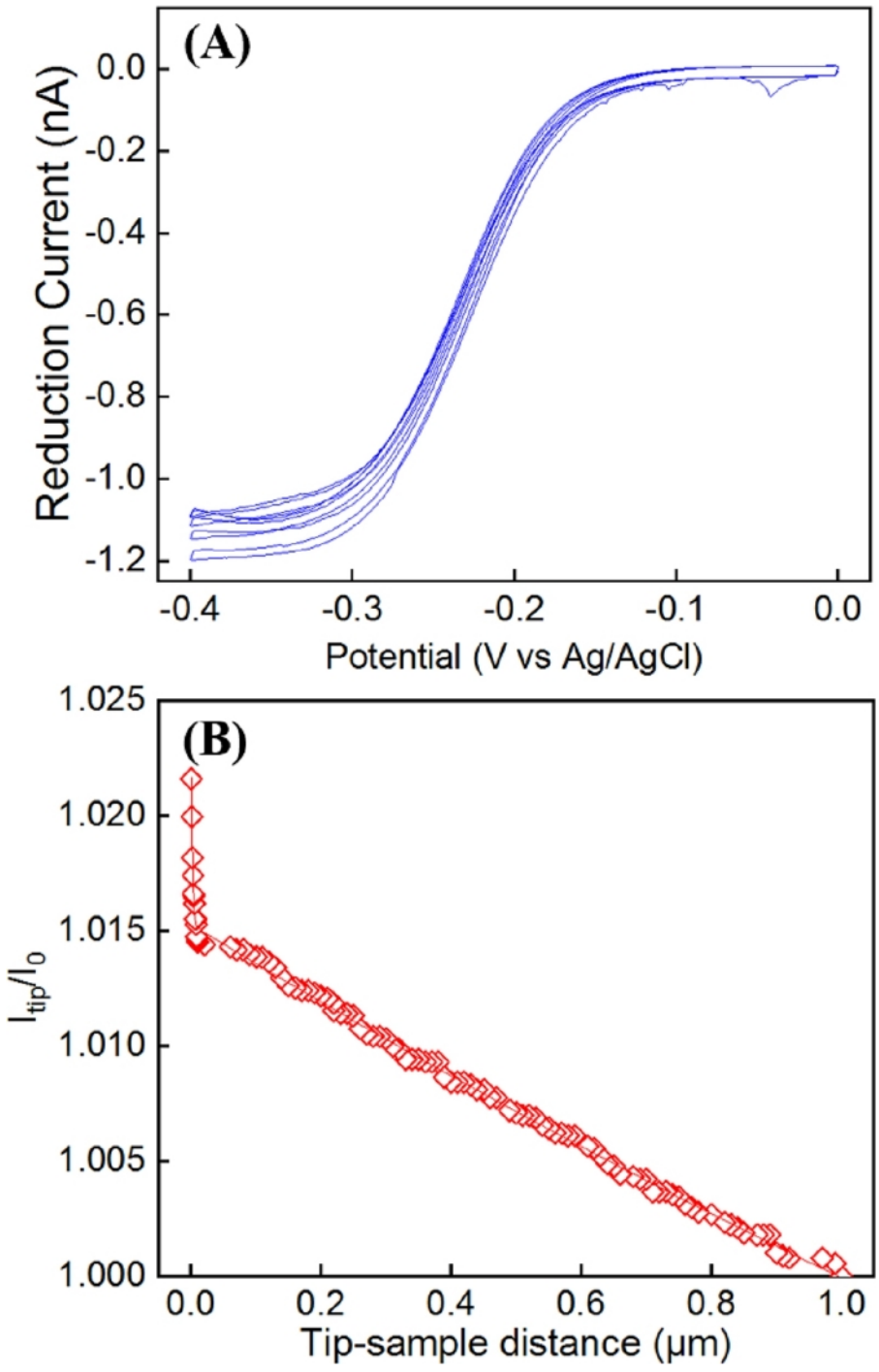

Figure 11: CV and Approach curves of Cu_2O NPs.

(**A**) Five CV scan in 10 mM $[Ru(NH_3)_6]^{3+}$ and 0.1 M KCl. (**B**) Approach curves of nanoelectrode probe on Cu_2O nanoparticle surface. Please click here to view a larger version of this figure.

Reaction	E_0 / V	Concentration	Applied Potential	Ref
$2H^+ + 2e^-$ H_2	0			
$[Ru(NH_3)_6]^{3+} + e^-$ $[Ru(NH_3)_6]^{2+}$	0.10 (NHE)	10 mM	−0.4 V (Ag/AgCl)	1
$2NO_2^- + 3H_2O + 4e^-$ $N_2O + 6OH^-$	0.15(NHE)	0.1 M	+0.95V (Ag/AgCl)	2
$[Fe(CN)_6]^{3-} + e^-$ $[Fe(CN)_6]^{4-}$	0.358(NHE)	2~5 mM	+0.0 ~ 0.5V(Ag/AgCl)	3
$ClO_4^- + H_2O + 2e^-$ $ClO_3^- + 2OH^-$	0.36(NHE)	0.1~1 M	+0.30 V(SCE)	4

$[IrCl_6]^{3-} + 3e^-$ ⇌ $Ir + 6Cl^-$	0.77(NHE)	10 mM	+1.0 V(Ag/AgCl)	5
$SO_4^{2-} + H_2O + 2e^-$ ⇌ $SO_3^{2-} + 2OH^-$	-0.93 (NHE)	10 mM	-0.45 V(Ag/AgCl)	6
$AgCl + e^-$ ⇌ $Ag + Cl^-$	0.22233(NHE)			

References:

1. Jiang, J. et al. Nanoelectrical and Nanoelectrochemical Imaging of Pt/ p-Si and Pt/p+-Si Electrodes. ChemSusChem. 10 (22), 4657-4663, (2017).

2. Izquierdo, J., Eifert, A., Kranz, C. & Souto, R. M. In situ monitoring of pit nucleation and growth at an iron passive oxide layer by using combined atomic force and scanning electrochemical microscopy. ChemElectroChem. 2 (11), 1847-1856, (2015).

3. Jones, C. E., Unwin, P. R. & Macpherson, J. V. In Situ Observation of the Surface Processes Involved in Dissolution from the Cleavage Surface of Calcite in Aqueous Solution Using Combined Scanning Electrochemical–Atomic Force Microscopy (SECM–AFM). ChemPhysChem. 4 (2), 139-146, (2003).

4. Anne, A., Cambril, E., Chovin, A., Demaille, C. & Goyer, C. Electrochemical atomic force microscopy using a tip-attached redox mediator for topographic and functional imaging of nanosystems. ACS nano. 3 (10), 2927-2940, (2009).

5. Macpherson, J. V., Jones, C. E., Barker, A. L. & Unwin, P. R. Electrochemical imaging of diffusion through single nanoscale pores. Analytical chemistry. 74 (8), 1841-1848, (2002).

6. Izquierdo, J., Eifert, A., Kranz, C. & Souto, R. M. In situ investigation of copper corrosion in acidic chloride solution using atomic force—scanning electrochemical microscopy. Electrochimica Acta. 247 588-599, (2017).

Table 1: Examples of redox mediators used in literature.

Figure S1: Photo showing connection between the bipotentiostat and the AFM controller. Please click here to download this figure.

Figure S2: Load the PeakForce SECM workspace in the software Please click here to download this figure.

Figure S3: Navigation panel for SECM workspace. Please click here to download this figure.

Figure S4: Run Open Circuit Potential – Time Please click here to download this figure.

Figure S5: Run Cyclic Voltammetry Please click here to download this figure.

Figure S6: Parameter setting for cyclic voltammetry measurement Please click here to download this figure.

Figure S7: Parameters for a Chronoamperometry measurement Please click here to download this figure.

Figure S8: Start current reading in AFM-SECM software Please click here to download this figure.

Figure S9: Parameters for Amperometric i-t technique Please click here to download this figure.

Discussion

A combined AFM-SECM technique that enables high-resolution multimodal imaging has been described in this protocol. This technique allows for topography to be mapped simultaneously with the SECM current collected or mapped on single nanoparticles or nanobubbles. Experiments were performed using commercial probes. These probes were designed to provide chemical compatibility with a wide range of electrochemical environments, electrochemical performance, mechanical stability, and multiple-cycle handling[18]. However, the stability and durability of the AFM-SECM are critical for the measurement of the electrochemical information with reliable and high resolution. As a result, the steps mentioned in steps 3.2 and 3.7 are critical to protecting the AFM-SECM tip from destroying by electrostatic discharge. Detailed discussion related to specific protocol steps are described as well.

In step 3.4.5, 10 mM $[Ru(NH_3)_6]^{3+}$ with supporting electrolyte of 0.1 M KCl was used in the presented test. 5-10 mM is a commonly used concentration of $[Ru(NH_3)_6]^{3+}$ in literature to obtain good current signals[30]. More examples of commonly used redox mediators in AFM-SECM measurements are summarized in the discussion (**Table 1**).

In step 3.4.6, the quality and stability of electrodes are confirmed with the OCP measurement. If the potential measured in OCP is not near zero or unstable, then the counter and pseudo-reference electrodes must be checked. The possible reasons for unstable OCP may be the

attachment of bubbles on the electrodes or the electrodes not immersed in liquid.

In step 3.4.8, the potential range mentioned here “High E” and “Low E” could be +0.3 V or −0.3 V of “init E/Final E” is a safe choice to start the CV test. Then, the potential range could be adjusted based on the potential value that led to a plateau current in the CV curve. Scan rate could vary between 0.01 V/s to 0.1 V/s. A higher scan rate attributes to a higher sensibility, but the charging current would also increase. Also, at high scan rates the voltammograms presented distorted shapes[64]. A higher sensitivity value should be selected as long as CV test does not show “overflow”. If an “overflow” message showed, then the sensitivity should be decreased.

In step 3.5.2, for imaging, the AFM-SECM imaging process was performed using a lift scan mode with a lift height typically 40-150 nm. If a lower lift height was selected, then there may be a possibility for tip crashing onto the sample surface. If the lift height was too high, then it may decrease the current imaging resolution since the tip is far away from the sample surface.

In step 3.5.3 in the presented measurement protocol, -0.4 V versus Ag/AgCl (-0.18V versus NHE) was chosen to perform the reduction of $[Ru(NH_3)_6]^{3+}$. The probe may reduce the $[Ru(NH_3)_6]^{3+}$ to $[Ru(NH_3)_6]^{2+}$ at -0.35 to -0.5 V vs Ag wire pseudo-reference electrode, while the sample maybe biased at 0 to -0.1 V for $[Ru(NH_3)_6]^{3+}$ regeneration. This value depends on the plateau current measured in the CV scan. It will also vary with different redox mediators as summarized in **Table 1**.

Also, the chronoamperometry technique was chosen because of the absence of Amperometric i-t technique in the presented bi-potentiostat. If readers have a bi-potentiostat that supports Amperometric i-t technique, they can set the i-t technique as shown in **Figure S9**. The run time was selected as 2000 seconds to make sure it is enough for at least one current imaging process in AFM-SECM.

Moreover, sample preparation is very important as well since the solid particles must be immobilized on the substrate completely so that particles do not detach during the imaging process. Moreover, to scan or probe electrochemical or electrical properties of sample surfaces (e.g., electrode), the binding between samples and substrates needs to ensure the electrical conductivity. The sample preparation methods should be useful and referable to a wide range of applications, especially for nano-objects characterization; however, sample immobilization methods may vary with specific samples[65,66]. Overall, we demonstrated that AFM-SECM enables high-resolution imaging of oxygen NBs and Cu_2O nanoparticles. Clearly, this AFM-SECM protocol is anticipated to play important roles in interfacial electrochemical analysis and will have broad applications in different research fields, such as material science, chemistry, and life science[1,19].

Disclosures

The authors have nothing to disclose.

Acknowledgments

This work is funded by the national science foundation (Award Number: 1756444) via Biological & Environmental Interfaces of Nano Materials, the USDA National Institute of Food and Agriculture, AFRI project [2018-07549] and Assistance Agreement No. 83945101-0 awarded by the U.S. Environmental Protection Agency to New Jersey Institute of Technology. It has not been formally reviewed by EPA. The views expressed in this document are solely those of authors

and do not necessarily reflect those of the Agency. EPA does not endorse any products or commercial services mentioned in this publication. The authors also thank Undergraduate Research and Innovation program (URI) Phase-1 & Phase-2 at New Jersey Institute of Technology.

References

1. Shi, X., Qing, W., Marhaba, T., Zhang, W. Atomic Force Microscopy-Scanning Electrochemical Microscopy (AFM-SECM) for Nanoscale Topographical and Electrochemical Characterization: Principles, Applications and Perspectives. *Electrochimica Acta.* 135472 (2019).
2. Aazam, E. S., Ghoneim, M. M., El-Attar, M. A. Synthesis, characterization, electrochemical behavior, and biological activity of bisazomethine dye derived from 2, 3-diaminomaleonitrile and 2-hydroxy-1-naphthaldehyde and its zinc complex. *Journal of Coordination Chemistry.* **64** (14), 2506-2520 (2011).
3. Shukla, A., Sampath, S., Vijayamohanan, K. Electrochemical supercapacitors: Energy storage beyond batteries. *Current science.* **79** (12), 1656-1661 (2000).
4. Kötz, R., Carlen, M. Principles and applications of electrochemical capacitors. *Electrochimica Acta.* **45** (15-16), 2483-2498 (2000).
5. Botte, G. G. Electrochemical manufacturing in the chemical industry. *The Electrochemical Society Interface.* **23** (3), 49-55 (2014).
6. Kongsricharoern, N., Polprasert, C. Electrochemical precipitation of chromium (Cr6+) from an electroplating wastewater. *Water Science and Technology.* **31** (9), 109-117 (1995).
7. Datta, M., Landolt, D. Fundamental aspects and applications of electrochemical microfabrication. *Electrochimica Acta.* **45** (15-16), 2535-2558 (2000).
8. Wang, S., George, K., Nesic, S. High pressure CO2 corrosion electrochemistry and the effect of acetic acid. *Corrosion/2004, paper.* **4375** (2004).
9. Song, G.L. in *Corrosion of Magnesium alloys.* 3-65 Elsevier, (2011).
10. Bellezze, T., Giuliani, G., Viceré, A., Roventi, G. Study of stainless steels corrosion in a strong acid mixture. Part 2: anodic selective dissolution, weight loss and electrochemical impedance spectroscopy tests. *Corrosion Science.* **130** 12-21 (2018).
11. Ehsani, A. et al. Evaluation of Thymus vulgaris plant extract as an eco-friendly corrosion inhibitor for stainless steel 304 in acidic solution by means of electrochemical impedance spectroscopy, electrochemical noise analysis and density functional theory. *Journal of Colloid and Interface Science.* **490** 444-451 (2017).
12. Cui, Z. H., Guo, X. X., Li, H. Equilibrium voltage and overpotential variation of nonaqueous Li–O2 batteries using the galvanostatic intermittent titration technique. *Energy & Environmental Science.* **8** (1), 182-187 (2015).
13. Elgrishi, N. et al. A Practical Beginner's Guide to Cyclic Voltammetry. *Journal of Chemical Education.* **95** (2), 197-206 (2018).
14. Amemiya, S., Bard, A. J., Fan, F.R. F., Mirkin, M. V., Unwin, P. R. Scanning Electrochemical Microscopy. *Annual Review of Analytical Chemistry.* **1** (1), 95-131 (2008).
15. Mirkin, M. V., Nogala, W., Velmurugan, J., Wang, Y. Scanning electrochemical microscopy in the 21st century.

Update 1: five years after. *Physical Chemistry Chemical Physics.* **13** (48), 21196-21212 (2011).

16. Bard, A. J., Fan, F. R. F., Kwak, J., Lev, O. Scanning electrochemical microscopy. Introduction and principles. *Analytical Chemistry.* **61** (2), 132-138 (1989).
17. Engstrom, R. C., Pharr, C. M. Scanning electrochemical microscopy. *Analytical Chemistry.* **61** (19), 1099A-1104A (1989).
18. Nellist, M. R. et al. Atomic force microscopy with nanoelectrode tips for high resolution electrochemical, nanoadhesion and nanoelectrical imaging. *Nanotechnology.* **28** (9), 095711 (2017).
19. Patel, A. N., Kranz, C. (Multi) functional atomic force microscopy imaging. *Annual Review of Analytical Chemistry.* **11** 329-350 (2018).
20. Ufheil, J., Heß, C., Borgwarth, K., Heinze, J. Nanostructuring and nanoanalysis by scanning electrochemical microscopy (SECM). *Physical Chemistry Chemical Physics.* **7** (17), 3185-3190 (2005).
21. Bergner, S., Wegener, J., Matysik, F.M. Simultaneous imaging and chemical attack of a single living cell within a confluent cell monolayer by means of scanning electrochemical microscopy. *Analytical Chemistry.* **83** (1), 169-174 (2011).
22. Hu, K. et al. Platinized carbon nanoelectrodes as potentiometric and amperometric SECM probes. *Journal of Solid State Electrochemistry.* **17** (12), 2971-2977 (2013).
23. Kranz, C. Recent advancements in nanoelectrodes and nanopipettes used in combined scanning electrochemical microscopy techniques. *Analyst.* **139** (2), 336-352 (2014).
24. Morris, C. A., Chen, C.C., Baker, L. A. Transport of redox probes through single pores measured by scanning electrochemical-scanning ion conductance microscopy (SECM-SICM). *Analyst.* **137** (13), 2933-2938 (2012).
25. Ludwig, M., Kranz, C., Schuhmann, W., Gaub, H. E. Topography feedback mechanism for the scanning electrochemical microscope based on hydrodynamic forces between tip and sample. *Review of Scientific Instruments.* **66** (4), 2857-2860 (1995).
26. Eckhard, K., Schuhmann, W. Alternating current techniques in scanning electrochemical microscopy (AC-SECM). *Analyst.* **133** (11), 1486-1497 (2008).
27. Macpherson, J. V., Unwin, P. R., Hillier, A. C., Bard, A. J. In-situ imaging of ionic crystal dissolution using an integrated electrochemical/AFM probe. *Journal of the American Chemical Society.* **118** (27), 6445-6452 (1996).
28. Huang, K., Anne, A., Bahri, M. A., Demaille, C. Probing Individual Redox PEGylated Gold Nanoparticles by Electrochemical–Atomic Force Microscopy. *ACS Nano.* **7** (5), 4151-4163 (2013).
29. Chennit, K. et al. Electrochemical Imaging of Dense Molecular Nanoarrays. *Analytical Chemistry.* **89** (20), 11061-11069 (2017).
30. Jiang, J. et al. Nanoelectrical and Nanoelectrochemical Imaging of Pt/p-Si and Pt/p+-Si Electrodes. *ChemSusChem.* **10** (22), 4657-4663 (2017).
31. Knittel, P., Mizaikoff, B., Kranz, C. Simultaneous nanomechanical and electrochemical mapping: combining peak force tapping atomic force microscopy with scanning electrochemical microscopy. *Analytical Chemistry.* **88** (12), 6174-6178 (2016).

32. Quist, A. P. et al. Atomic force microscopy imaging and electrical recording of lipid bilayers supported over microfabricated silicon chip nanopores: Lab-on-a-chip system for lipid membranes and ion channels. *Langmuir.* **23** (3), 1375-1380 (2007).
33. Cohen, H. et al. Electrical characterization of self-assembled single- and double-stranded DNA monolayers using conductive AFM. *Faraday Discussions.* **131** (0), 367-376 (2006).
34. Chung, J. W. et al. Single-crystalline organic nanowires with large mobility and strong fluorescence emission: a conductive-AFM and space-charge-limited-current study. *Journal of Materials Chemistry.* **19** (33), 5920-5925 (2009).
35. Guo, D.Z., Hou, S.M., Zhang, G.M., Xue, Z.Q. Conductance fluctuation and degeneracy in nanocontact between a conductive AFM tip and a granular surface under small-load conditions. *Applied Surface Science.* **252** (14), 5149-5157 (2006).
36. Rocca, E., Bertrand, G., Rapin, C., Labrune, J. C. Inhibition of copper aqueous corrosion by non-toxic linear sodium heptanoate: mechanism and ECAFM study. *Journal of Electroanalytical Chemistry.* **503** (1), 133-140 (2001).
37. Toma, F. M. et al. Mechanistic insights into chemical and photochemical transformations of bismuth vanadate photoanodes. *Nature Communications.* **7** 12012-12012 (2016).
38. Kouzeki, T., Tatezono, S., Yanagi, H. Electrochromism of Orientation-Controlled Naphthalocyanine Thin Films. *The Journal of Physical Chemistry.* **100** (51), 20097-20102 (1996).
39. Yamaguchi, Y., Shiota, M., Nakayama, Y., Hirai, N., Hara, S. Combined in situ EC-AFM and CV measurement study on lead electrode for lead–acid batteries. *Journal of Power Sources.* **93** (1), 104-111 (2001).
40. Comstock, D. J., Elam, J. W., Pellin, M. J., Hersam, M. C. Integrated Ultramicroelectrode−Nanopipet Probe for Concurrent Scanning Electrochemical Microscopy and Scanning Ion Conductance Microscopy. *Analytical Chemistry.* **82** (4), 1270-1276 (2010).
41. Ebejer, N., Schnippering, M., Colburn, A. W., Edwards, M. A., Unwin, P. R. Localized High Resolution Electrochemistry and Multifunctional Imaging: Scanning Electrochemical Cell Microscopy. *Analytical Chemistry.* **82** (22), 9141-9145 (2010).
42. Ebejer, N. et al. Scanning Electrochemical Cell Microscopy: A Versatile Technique for Nanoscale Electrochemistry and Functional Imaging. *Annual Review of Analytical Chemistry.* **6** (1), 329-351 (2013).
43. Alheshibri, M., Qian, J., Jehannin, M., Craig, V. S. A history of nanobubbles. *Langmuir.* **32** (43), 11086-11100 (2016).
44. Liu, G., Wu, Z., Craig, V. S. Cleaning of protein-coated surfaces using nanobubbles: an investigation using a quartz crystal microbalance. *The Journal of Physical Chemistry C.* **112** (43), 16748-16753 (2008).
45. Ghadimkhani, A., Zhang, W., Marhaba, T. Ceramic membrane defouling (cleaning) by air Nano Bubbles. *Chemosphere.* **146** 379-384 (2016).
46. Uchida, T. et al. Transmission electron microscopic observations of nanobubbles and their capture of impurities in wastewater. *Nanoscale Research Letters.* **6** (1), 1 (2011).

47. Ushikubo, F. Y. et al. Evidence of the existence and the stability of nano-bubbles in water. *Colloids and Surfaces A: Physicochemical and Engineering Aspects.* **361** (1-3), 31-37 (2010).
48. Bowley, W. W., Hammond, G. L. Controlling factors for oxygen transfer through bubbles. *Industrial, Engineering Chemistry Process Design and Development.* **17** (1), 2-8 (1978).
49. Li, P., Takahashi, M., Chiba, K. Enhanced free-radical generation by shrinking microbubbles using a copper catalyst. *Chemosphere.* **77** (8), 1157-1160 (2009).
50. Takahashi, M. et al. Effect of shrinking microbubble on gas hydrate formation. *The Journal of Physical Chemistry B.* **107** (10), 2171-2173 (2003).
51. Takahashi, M., Chiba, K., Li, P. Free-radical generation from collapsing microbubbles in the absence of a dynamic stimulus. *The Journal of Physical Chemistry B.* **111** (6), 1343-1347 (2007).
52. Ahmed, A. K. A. et al. Influences of air, oxygen, nitrogen, and carbon dioxide nanobubbles on seed germination and plant growth. *Journal of Agricultural and Food Chemistry.* **66** (20), 5117-5124 (2018).
53. Zhang, D.F. et al. Delicate control of crystallographic facet-oriented Cu 2 O nanocrystals and the correlated adsorption ability. *Journal of Materials Chemistry.* **19** (29), 5220-5225 (2009).
54. Khaled Abdella Ahmed, A. et al. Colloidal Properties of Air, Oxygen, and Nitrogen Nanobubbles in Water: Effects of Ionic Strength, Natural Organic Matters, and Surfactants. *Environmental Engineering Science.* (2017).
55. Huang, Z. et al. PeakForce scanning electrochemical microscopy with nanoelectrode probes. *Microscopy Today.* **24** (6), 18-25 (2016).
56. Lou, S.T. et al. Nanobubbles on solid surface imaged by atomic force microscopy. *Journal of Vacuum Science, Technology B: Microelectronics and Nanometer Structures Processing, Measurement, and Phenomena.* **18** (5), 2573-2575 (2000).
57. Borkent, B. M., Dammer, S. M., Schönherr, H., Vancso, G. J., Lohse, D. Superstability of surface nanobubbles. *Physical Review Letters.* **98** (20), 204502 (2007).
58. Agarwal, A., Ng, W. J., Liu, Y. Principle and applications of microbubble and nanobubble technology for water treatment. *Chemosphere.* **84** (9), 1175-1180 (2011).
59. Tasaki, T., Wada, T., Baba, Y., Kukizaki, M. Degradation of surfactants by an integrated nanobubbles/VUV irradiation technique. *Industrial & Engineering Chemistry Research.* **48** (9), 4237-4244 (2009).
60. Fujita, D., Itoh, H., Ichimura, S., Kurosawa, T. Global standardization of scanning probe microscopy. *Nanotechnology.* **18** (8), 084002 (2007).
61. Häßler-Grohne, W., Hüser, D., Johnsen, K.P., Frase, C. G., Bosse, H. Current limitations of SEM and AFM metrology for the characterization of 3D nanostructures. *Measurement Science and Technology.* **22** (9), 094003 (2011).
62. Sakai, K. in *Measurement Techniques and Practices of Colloid and Interface Phenomena.* 51-57 Springer, (2019).
63. Gan, T., Wu, B., Zhou, X., Zhang, G. Ultrahigh resolution, serial fabrication of three dimensionally-patterned protein nanostructures by liquid-mediated non-contact scanning

probe lithography. *RSC Advances.* **6** (55), 50331-50335 (2016).

64. Arteaga, J. F. et al. Comparison of the simple cyclic voltammetry (CV) and DPPH assays for the determination of antioxidant capacity of active principles. *Molecules.* **17** (5), 5126-5138 (2012).

65. Moreno-Herrero, F., Colchero, J., Gomez-Herrero, J., Baro, A. Atomic force microscopy contact, tapping, and jumping modes for imaging biological samples in liquids. *Physical Review E.* **69** (3), 031915 (2004).

66. Doktycz, M. et al. AFM imaging of bacteria in liquid media immobilized on gelatin coated mica surfaces. *Ultramicroscopy.* **97** (1-4), 209-216 (2003).